

1 **Impacts of the January 2022 Tonga volcanic eruption on**
2 **the ionospheric dynamo: ICON-MIGHTI and Swarm**
3 **observations of extreme neutral winds and currents**

4 **Brian J. Harding¹, Yen-Jung Joanne Wu¹, Patrick Alken², Yosuke Yamazaki³,**
5 **Colin C. Triplett¹, Thomas J. Immel¹, L. Claire Gasque¹, Stephen B. Mende¹,**
6 **Chao Xiong⁴**

7 ¹Space Sciences Laboratory, University of California Berkeley, Berkeley, CA, USA

8 ²University of Colorado, Boulder, CO, USA

9 ³GFZ German Research Centre for Geosciences, Potsdam, Germany

10 ⁴Department of Space Physics, Electronic Information School, Wuhan University, 430072 Wuhan, China

11 **Key Points:**

- 12 • Extreme thermospheric winds and ionospheric currents were observed in coordi-
13 nated space/ground-based measurements, ten hours post-eruption
- 14 • The westward electrojet current when the Lamb wave reaches the dayside is con-
15 sistent with recent studies of the wind-driven electrojet
- 16 • Observations of linked dynamo processes provide direct evidence of the space-weather
17 impacts of acute lower atmospheric forcing

Corresponding author: Brian J. Harding, bharding@ssl.berkeley.edu

Abstract

The eruption of the Hunga Tonga-Hunga Ha’apai volcano on 15 January 2022 triggered atmospheric waves at all altitudes. The NASA Ionospheric Connection Explorer (ICON) and ESA Swarm satellites were well placed to observe its impact on the ionospheric wind dynamo. After the Lamb wave entered the dayside, Swarm A observed an eastward and then westward equatorial electrojet (EEJ) on two consecutive orbits, each with magnitudes exceeding the 99.9th percentile of typically observed values. ICON simultaneously observed the neutral wind (90–300 km altitude) at approximately the same distance from Tonga. The observed neutral winds were also extreme (>99.9th percentile at some altitudes). The covariation of EEJ and winds is consistent with recent theoretical and observational results, indicating that the westward electrojet is driven by strong westward winds in the Pedersen region (~120–150 km). These observations imply that the dynamo is a key mechanism in the ionospheric response to the Tonga disturbance.

Plain Language Summary

The January 2022 Tonga volcanic eruption caused atmospheric impacts around the world. As a natural experiment, it can be used to test our understanding of how the lower atmosphere affects space weather. Researchers are only beginning to document the chain of events post-eruption, and this paper focuses on its impact on the generator that drives electric fields in near-Earth space, a key part of space weather. This generator is driven by the atmosphere pushing charged particles across Earth’s magnetic field. This usually creates a strong eastward current above the equator. When the Swarm A satellite coincided with the wave from Tonga, it observed that this current strengthened dramatically, then reversed. Although reversals are not unusual, this was the strongest reversal observed by Swarm since its 2013 launch, except for one large geomagnetic storm in 2015. Another satellite, the Ionospheric Connection Explorer, was luckily at the right time and place to observe related motions of the upper atmosphere, which were similarly extreme. These observations are shown to be consistent with our theoretical understanding of the generator. This study is important because it represents a critical test of atmosphere-space interactions and implies that the Tonga eruption caused a major space weather event.

1 Introduction

Isolated disturbances such as earthquakes, tsunamis, and solar eclipses, as well as explosions from volcanoes, nuclear detonations, and meteor air bursts can offer discrete tests for models of atmosphere-ionosphere coupling and variability (Aryal et al., 2020; Astafyeva, 2019; Inchin, Snively, et al., 2020; Li et al., 2021; Zettergren & Snively, 2019). The Hunga Tonga-Hunga Ha’apai (hereafter Tonga) volcanic eruption on 15 Jan 2022 generated atmospheric disturbances from the ground to the ionosphere (Adam, 2022; Wright et al., 2022). A typical wave mode excited by impulsive events in the lower atmosphere is the Lamb wave, an acoustic nondispersive edge wave (Garrett, 1969; Bretherton, 1969; Nishida et al., 2014). The study by Wright et al. (2022) presented data from the troposphere, stratosphere, and mesosphere, showing a coherent wave propagating at 318 m/s around the globe multiple times, identified as a Lamb wave. Although the Lamb wave propagates in the troposphere, energy leaks into higher altitudes, exciting other wave modes, in which the amplitude of wind, temperature, and pressure fluctuations can grow with altitude (Nishida et al., 2014; Wright et al., 2022). As such, the ionosphere, readily observed by ground-based instruments, can function as a sensitive monitor of atmospheric disturbances.

Initial Total Electron Content (TEC) observations have reported Traveling Ionospheric Disturbances (TIDs) propagating globally for many hours and even days after the Tonga eruption (Aa et al., 2022; Lin et al., 2022; Themens et al., 2022; Zhang et al.,

2022). Estimates of the horizontal wavelength of TIDs in the far field (i.e., at distances >3000 km from the eruption) range from 300 to 1000 km (Wright et al., 2022; Zhang et al., 2022). Additionally, Soares et al. (2022) reported oscillations of the geomagnetic field observed by a ground-based magnetometer 835 km from Tonga, which are attributed to short-period modulation (3-5 min) of ionospheric currents. No studies have yet reported data connecting the homosphere with these ionospheric signatures.

The mechanisms through which signals from the lower atmosphere are transmitted and create observable effects in the ionosphere are numerous, and understanding their complex interplay is critical for interpreting and predicting ionospheric signals. These mechanisms include those resulting from direct propagation of the wave or waves to ionospheric *F*-region heights, modifying ion drag and/or plasma loss rates. Another mechanism is indirect, mediated by electric fields resulting from the neutral wind dynamo, which can carry signatures along magnetic field lines from the *E* region to the *F* region. Wright et al. (2022) presented ionospheric TIDs with phase speeds, horizontal wavelengths, and arrival times inconsistent with the Lamb wave, speculating that the observed TEC signatures likely arrived by indirect paths from Tonga. The signal can also be transmitted to the opposite hemisphere, which has been proposed to explain the appearance of TIDs over Japan ahead of the Lamb wave (Lin et al., 2022). Conjugate effects were also suggested by Themens et al. (2022). In this study we report on two aspects of the Tonga disturbance: neutral winds and ionospheric dynamo signatures.

Specifically, we report extreme perturbations in the equatorial electrojet (EEJ) observed by Swarm and extreme perturbations in neutral winds from 90 to 300 km altitude observed by the Michelson Interferometer for Global High-resolution Thermospheric Imaging (MIGHTI) on the Ionospheric Connection Explorer (ICON) (Immel et al., 2018). The EEJ is an intense band of zonal electric current confined near the magnetic equator flowing in the daytime between \sim 90 and 120 km altitude (Yamazaki & Maute, 2017, and references therein). Variations in the EEJ closely track those of the equatorial zonal electric field (i.e., vertical plasma drift) which has widespread effects on the equatorial ionosphere by modifying the production-loss-transport balance. Typically the EEJ flows eastward, associated with an eastward zonal electric field, upward drift, and enhanced equatorial fountain effect, but sometimes the EEJ flows westward, associated with the opposite ionospheric conditions. In the absence of direct solar insolation, the EEJ disappears at night.

ICON and Swarm have been operating simultaneously since ICON's launch in 2019, offering an unprecedented observational capability for studies related to the ionospheric dynamo. On 15 Jan 2022, their orbits were unusually well-synced to provide complementary observations of the Tonga signature, as discussed below. This study does not attempt to quantify properties or classifications of the waves excited by the Tonga explosion, which will undoubtedly be a focus of future investigations. However, the unique opportunity created by coincident observations of the neutral wind by MIGHTI and ionospheric currents by Swarm allows us to directly study the impact of these waves on the ionospheric dynamo, which we report here. In addition, four magnetometer sites are utilized to provide a ground-based perspective on the EEJ variation.

2 Data sources

2.1 ICON-MIGHTI neutral winds

This study uses neutral wind data from the MIGHTI instrument on the ICON spacecraft, which is in a 27° inclination orbit. Neutral wind profiles (ICON data product 2.2 v04) from 90 to 300 km altitude are derived from remote observations of green 557.7 nm and red 630.0 nm airglow emissions. More information on MIGHTI can be found in previous instrument and validation papers (Englert et al., 2017; Harding et al., 2017, 2021;

118 Makela et al., 2021). Dayside data only are considered, because the EEJ vanishes at night.
 119 Below 180 km altitude, we use samples from the green channel, which are preprocessed
 120 to improve precision by binning vertically by a factor of 2, yielding ~ 6 km sampling. Above
 121 180 km, we use samples from the red channel.

122 Although the focus is on two orbits on 15 Jan 2022, we also make use of the entire
 123 dataset for background statistics. Specifically, we use all MIGHTI profiles from the
 124 start of the mission until 14 Jan 2022 for which the variable “Wind_Quality” is equal
 125 to 1 (i.e., highest quality, 1,086,830 profiles in total). To generate these statistics, in ad-
 126 dition to the altitude binning discussed above, the data were preprocessed with a 5-sample
 127 median filter in time to remove outliers. Data obtained during geomagnetic storms are
 128 included in these statistics. Statistics are presented in terms of percentiles; for example,
 129 the 90% level for zonal wind represents a value such that 10% of samples have a zonal
 130 wind larger than that level.

131 2.2 Swarm A EEJ current

132 The Swarm constellation comprises three satellites in near-polar orbits. In this study
 133 we use EEJ intensity estimates from one spacecraft, Swarm A, which flies at an altitude
 134 of ~ 440 km with an inclination of 87.4° . Latitude-dependent height-integrated EEJ in-
 135 tensity is provided by the Swarm Level 2 Product EEF (Eastward Electric Field) (Alken
 136 et al., 2013). The EEJ current is estimated from magnetometer measurements during
 137 every dayside overflight of the magnetic equator (Alken, 2020). Ground-based valida-
 138 tion is discussed by Alken et al. (2015).

139 In a manner analogous to the wind analysis, background statistics are calculated
 140 for context, using the entire available dataset. Specifically, we use the version 0204 dataset
 141 spanning 25 Nov 2013 to 14 Jan 2022. We first preprocess the EEJ data to remove non-
 142 physical current distributions. These outliers are identified by computing the the total
 143 “off-peak current” for each overflight (defined as the root-mean-square of currents pole-
 144 ward of 5 deg quasidipole latitude). Overflights are removed if the off-peak current is larger
 145 than 100 times the interquartile range of all the overflights (i.e., 75th percentile minus
 146 25th percentile). This removes 25 overflights which are, by visual inspection, clear non-
 147 physical outliers. The 45,184 remaining overflights are used in the statistics below. All
 148 data on 15 Jan 2022 remain after this preprocessing step.

149 2.3 Ground-based magnetometers

150 We also use ground-based magnetometer data to support the interpretation of the
 151 EEJ behavior on 15 Jan 2022. The intensity of the EEJ can be estimated using the hor-
 152 izontal (H) component of the geomagnetic field observed at two stations, one being lo-
 153 cated at the magnetic equator and the other located about the same longitude but out-
 154 side the EEJ band (Anderson et al., 2004). The difference in H (ΔH) at the two stations,
 155 after subtracting the nighttime baseline, represents the EEJ intensity. We use data from
 156 Huancayo (HUA, 12.0°S , 75.3°W) and Piura (PIU, 5.2°S , 80.6°W) for the Peruvian sec-
 157 tor, and Tatuoca (TTB, 1.2°S , 48.5°W) and Kourou (KOU, 5.2°N , 52.7°W) for the Brazil-
 158 ian sector. These stations are positioned to detect EEJ signatures in the vicinity of the
 159 Swarm observations.

160 3 Results and Discussion

161 3.1 Data selection and observational geometry

162 The Tonga volcanic eruption occurred around 04:15 UT on 15 Jan 2022, near lo-
 163 cal sunset. Since the tropospheric sound speed is slower than the Earth’s rotation at these
 164 latitudes, the Lamb wave was mostly contained to the dusk and nighttime sectors for

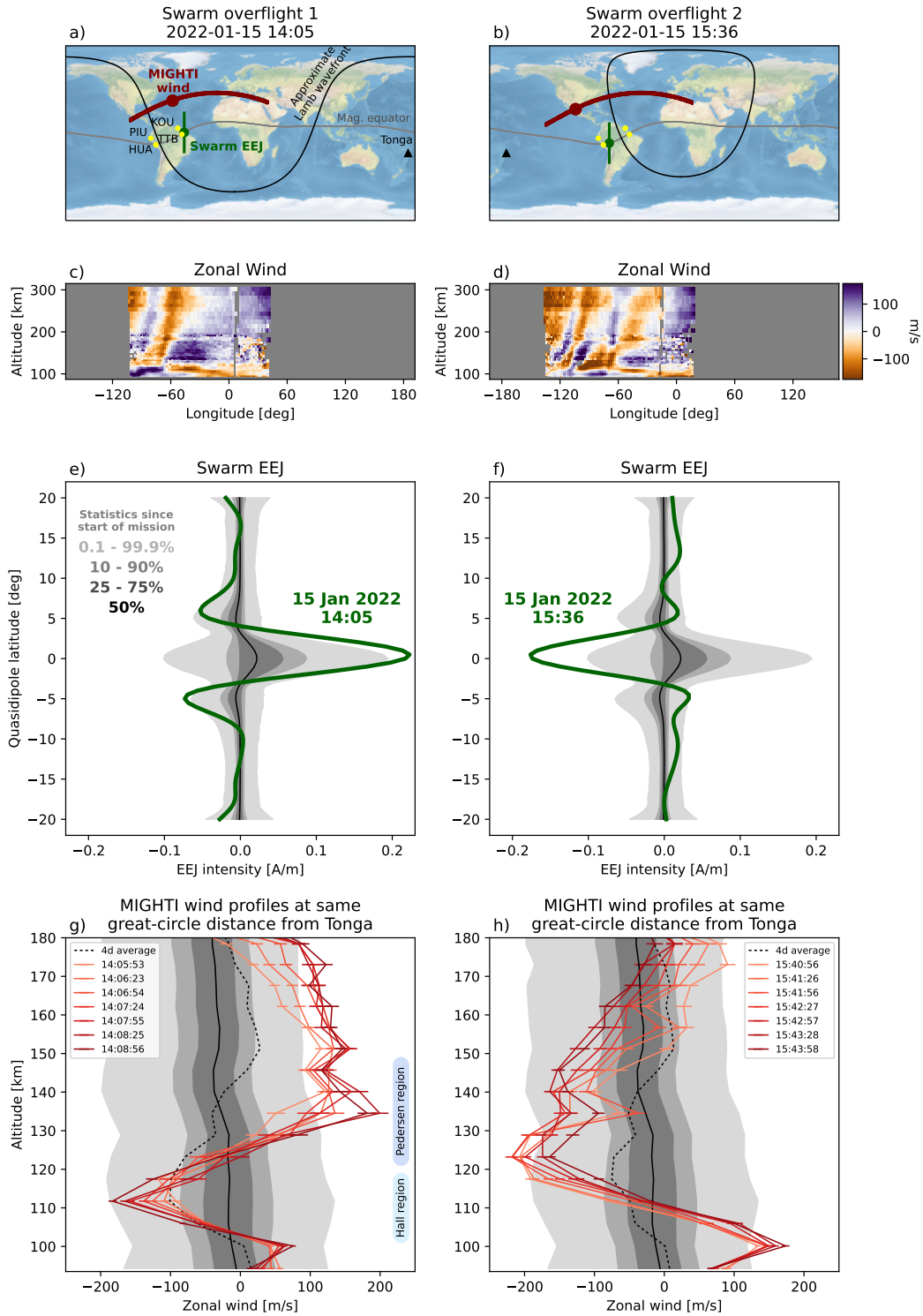


Figure 1. (a,b) Locations of ICON-MIGHTI wind (red), Swarm EEJ (green), ground-based magnetometers (yellow), and a wavefront from Tonga moving at 318 m/s (black), for two selected orbits. Dots denote locations at the given time. (c,d) Zonal wind profiles (positive eastward) at the same locations above. (e,f) Swarm A EEJ observations on each orbit. (g,h) MIGHTI zonal wind profiles on each orbits, chosen to correspond to samples at the same great-circle distance from Tonga as the Swarm observation, for assumed wave velocities spanning 300–330 m/s. Background statistics (gray shaded areas and black solid line) represent percentiles of the entire dataset. The background wind (black dotted line) is estimated from the four previous days (see text).

165 the first several hours after the eruption. In this study we focus on thermosphere-ionosphere
 166 signatures once the wave reaches the dayside, where ionospheric currents are strongest.
 167 According to the parameters reported by Wright et al. (2022) (318 m/s phase speed orig-
 168 inating in Tonga at 04:28 UT), the lower atmospheric Lamb wave reached the dayside
 169 around 13 UT at low/mid-latitudes. Amores et al. (2022) provide further information
 170 on the Lamb wave propagation, including a numerical simulation which agrees with the
 171 timing used here. The Lamb wave entered the dayside in the American longitude sec-
 172 tor. Serendipitously, Swarm A overflights occurred in this sector at 14:05 UT and 15:36
 173 UT. In this study we utilize data from these two orbits and the corresponding orbits of
 174 ICON, which samples all longitudes every orbit, albeit at different latitudes.

175 The two orbits are shown in Figure 1, an animated version of which can be found
 176 in the Supporting Information (Movie S1). For context, we show a reference wavefront
 177 using the Lamb wave parameters reported by Wright et al. (2022). Given the close align-
 178 ment between ICON and Swarm, these parameters are not important for our conclusions,
 179 and similar parameters (e.g., a 310 m/s wavefront originating at 04:15 UT) do not change
 180 the interpretation. On the first orbit (panel a), Swarm A crossed the equator and mea-
 181 sured the EEJ at a location roughly 3000 km ahead of the 318 m/s wavefront. At the
 182 time Swarm A measured the EEJ at the equator, MIGHTI sampled the wind ~ 35 de-
 183 grees farther north but at a similar great-circle distance from Tonga.

184 The next orbit is shown to the right (panel b). On this orbit, Swarm A measured
 185 the EEJ at a location roughly 1500 km behind the assumed 318 m/s wavefront. At the
 186 time of the Swarm A overflight, MIGHTI samples the wind roughly 3500 km behind the
 187 wavefront, but reached the same great-circle distance as Swarm A 5 minutes later (15:41
 188 UT).

189 In both orbits, the MIGHTI data (panels c and d) show large zonal wind fluctu-
 190 ations, vertical shears, and coherent wave structures spanning at least 110–300 km, both
 191 ahead of and behind the 318 m/s wavefront. Above 120 km, the horizontal wavelengths
 192 of the wave structures are estimated by visual inspection to be 3000–5000 km, more than
 193 three times as large as the horizontal wavelengths reported in TEC observations in the
 194 far field. It is apparent from these observations that the thermospheric signatures of this
 195 event are complex and likely not explained by a single wave mode. We do not comment
 196 further on the wind features in this paper, but instead we focus on their impact on iono-
 197 spheric currents in the next section.

198 Although the meridional wind fluctuations are in some cases quite significant (not
 199 shown), we focus on zonal winds because (1) meridional winds are nearly parallel to the
 200 magnetic field at the equator and are not expected to strongly influence the EEJ, and
 201 (2) the wave is propagating nearly zonally in this region. The dominant large-scale sig-
 202 nature of the wave is therefore expected to be in the zonal wind. A separate analysis was
 203 conducted where the zonal and meridional winds were combined to calculate the radial
 204 wind perturbation in the direction away from Tonga. However, this yielded identical con-
 205 clusions and was more complicated to compare quantitatively with background statis-
 206 tics.

207 **3.2 Comparison between MIGHTI winds and Swarm EEJ**

208 The bottom two rows of Figure 1 compare directly the Swarm A EEJ observations
 209 with the MIGHTI wind observations on these two orbits. On the first orbit (panel e),
 210 Swarm A observed an extremely strong eastward EEJ (0.22 A/m). This represents the
 211 strongest EEJ observed by Swarm A since 2017, and the 19th strongest overall (stronger
 212 than 99.96% of all observations in the Swarm A dataset, which started in 2013). On the
 213 next orbit (panel f), Swarm A observes an extreme westward EEJ (-0.17 A/m), often
 214 referred to as a counter-electrojet. Except for three overflights during the 22-23 June 2015
 215 geomagnetic storm, this represents the strongest westward EEJ in the Swarm A dataset.

216 Swarm A data from earlier orbits on this day do not show variations above the 90% level.
 217 Also shown are statistics computed from all EEJ observations from the start of the mis-
 218 sion until 14 Jan 2022. The black line is the median, the dark gray shaded region is the
 219 interquartile range (25–75%), and other percentile ranges are shown in lighter gray. Al-
 220 though Swarm B is not included in this quantitative analysis, data from Swarm B also
 221 show a large positive EEJ (0.20 A/m) followed by a large negative EEJ (-0.14 A/m) on
 222 these two orbits (not shown). Swarm C flies in a side-by-side configuration to Swarm A,
 223 and recorded similar measurements on these two orbits (0.22 A/m and -0.17 A/m respec-
 224 tively, not shown).

225 The bottom of Figure 1 (panels g and h) shows the MIGHTI zonal wind profiles
 226 corresponding to the Swarm A EEJ observations, compared with background variabil-
 227 ity shown with statistical ranges in gray, analogous to panels e and f. Zonal wind pro-
 228 files (shown in red) are chosen such that their distance from Tonga is identical to Swarm
 229 A’s distance when it crossed the magnetic equator. Insofar as the wave can be assumed
 230 to propagate concentrically, this is a proxy for the neutral wind fluctuations in the equa-
 231 torial region during the Swarm A overflight. The various profiles in Figure 1 are chosen
 232 to provide exact alignment for assumed wave velocities ranging from 300 to 330 m/s.

233 The qualitative similarity of these profiles suggests that this procedure to align the
 234 Swarm and MIGHTI observations is not significantly sensitive to the assumed wave ve-
 235 locity, a consequence of the fortunate timing of the two observations. The temporal off-
 236 sets required are 0–8 minutes, a time scale that is not likely of importance for the large-
 237 scale waves observable by MIGHTI. Furthermore, it is the same magnitude as the as-
 238 sumption of temporal persistence used to produce the vector wind estimate by combin-
 239 ing the data from the two MIGHTI sensors (5–9 minutes) (Harding et al., 2017). A pos-
 240 sibly non-negligible uncertainty in this procedure is the assumption of concentric wave
 241 propagation, as the two observations sample along different wave azimuths from Tonga,
 242 separated by 5–32 degrees.

243 These zonal wind profiles are a superposition of the volcanogenic waves and the back-
 244 ground thermospheric state upon which they propagate. The black dashed line is an es-
 245 timate of that background state, computed from an average of profiles at nearly the same
 246 local time (± 1 hr) and longitude (± 24 deg, the amount of Earth rotation in one ICON
 247 orbit) as the profiles shown. This average is generated using the 4 previous days (Jan
 248 11–14), over which time the sampled latitude changes by no more than 10 deg. It is thus
 249 an estimate of the contribution from background migrating and non-migrating tides and
 250 planetary waves with periods $\gtrsim 8$ days. However, there may also be contributions to the
 251 background from short-term tidal variability, short-period planetary waves like the quasi-
 252 two-day wave, and geomagnetic activity, which are difficult to comprehensively quan-
 253 tify from a single observatory.

254 The wind profiles on both orbits are extreme, showing values comparable with, or
 255 stronger than, the 0.1% and 99.9% levels. We describe the wind profile in terms of two
 256 regions: The “Hall region,” (~ 100 – 120 km) where the Hall conductivity is large and dom-
 257 inant, and the “Pedersen region,” (~ 120 – 150 km) where the Pedersen conductivity is large
 258 and dominant. In reality the Hall and Pedersen conductivities are nonzero over larger
 259 altitude ranges, and there is a significant overlap region in which they are both large;
 260 however, this description is useful to connect with theoretical arguments below. On or-
 261 bit 1, when the EEJ is strongly eastward, MIGHTI observes a westward wind in the Hall
 262 region, which is not unusual compared to the background profile. However, there is also
 263 a strong eastward wind in the Pedersen region which exceeds the 99.9% level. Indeed,
 264 this represents the strongest wind observed at ~ 140 km since the start of the mission.
 265 On orbit 2, when the EEJ is strongly westward, MIGHTI observes an eastward wind,
 266 peaking around 100 km in the lower Hall region, and a westward wind above ~ 110 km,
 267 which spans the upper Hall region and the Pedersen region. This profile is unusual rel-
 268 ative to the background wind and exceeds the 99.9% level at some altitudes.

269 This correspondence between the EEJ and neutral winds is consistent with the re-
 270 lationship developed by Yamazaki et al. (2014) and Yamazaki et al. (2021). The early
 271 theoretical literature on the EEJ suggested that while height-varying local winds influ-
 272 ence the currents outside the EEJ, they are not expected to have a significant influence
 273 on the EEJ itself, because it is dominated by the influence of the global zonal electric
 274 field (Richmond, 1973). However, the modeling study by Yamazaki et al. (2014) predicted
 275 that winds should have a significant role and that the EEJ should be negatively corre-
 276 lated with Hall-region zonal winds and positively correlated with Pedersen-region winds.
 277 This was observationally confirmed with the availability of concurrent MIGHTI and Swarm
 278 observations by Yamazaki et al. (2021). The implicated mechanism is local generation
 279 of electric fields which was not considered explicitly in the early (pre-2000) literature:
 280 (1) in the Hall region, an eastward wind drives eastward current, which generates a west-
 281 ward electric field; (2) in the Pedersen region, an eastward wind drives upward current,
 282 which generates a downward electric field. At the footpoint of this field line, which lies
 283 in the Hall region, the westward currents driven by this electric field will generate an east-
 284 ward electric field. Since the EEJ current flows in the Hall region, Pedersen-region driv-
 285 ing is a noteworthy example of winds outside the EEJ perturbing currents in the EEJ.

286 In orbit 1, the strong westward Hall-region wind and strong eastward Pedersen-region
 287 wind is expected to cause a strong eastward EEJ through the Yamazaki et al. (2014) re-
 288 lationship. In orbit 2, the Hall-region wind is eastward below 110 km and westward above
 289 110 km, which is expected to yield minimal total forcing in the Hall region. However,
 290 the Pedersen-region wind is strongly westward, which is expected to cause a strong west-
 291 ward EEJ. In both cases, the Swarm observations match the expectation. This result
 292 confirms the Yamazaki relationship holds under extreme conditions. More interestingly,
 293 because the Hall-region effect is small in orbit 2, the EEJ is apparently driven mostly
 294 by winds at higher altitudes, confirming the importance of nonlocal wind driving of the
 295 EEJ. The current paths that regulate this control deserve further inquiry, both obser-
 296 vationally and theoretically.

297 3.3 Ground-based magnetometer data

298 In this section we report EEJ observations from two pairs of magnetometers located
 299 near the Swarm overflights (see Figure 1). The observations are shown in the first two
 300 panels of Figure 2 using blue lines. The black line shows the monthly mean, and the gray
 301 shaded area represents 1 standard deviation (i.e., 1σ) above and below the mean.

302 The HUA-PIU pair in Peru observes a negative ΔH (corresponding to a westward
 303 EEJ) beginning around 12 UT, lasting until just after 16 UT (except for one brief pe-
 304 riod of weak eastward EEJ near 15 UT). The TTB-KOU pair in Brazil observes an east-
 305 ward EEJ until ~ 15 UT, followed by a period of westward EEJ until 18 UT. Superim-
 306 posed on these broad patterns are shorter, 1-hour-scale features which are discussed in
 307 the next section.

308 The broad features and relative timing seen in the magnetometer data are qual-
 309 itatively consistent with the Swarm observations. Namely, a negative disturbance is first
 310 seen over Peru, then over Brazil 2–4 hours later, consistent with eastward propagation.
 311 The presence of 1-hour-scale fluctuations and the lack of EEJ before sunrise makes it dif-
 312 ficult to estimate the relative timing with greater accuracy. On the first Swarm overflight
 313 at 14:05 UT, the nearby Brazilian pair observes an eastward EEJ which is 1σ or less above
 314 the climatology. On the second Swarm overflight at 15:36 UT, the Peruvian pair observes
 315 a $\sim 2.5\sigma$ extreme westward EEJ. Especially for the positive EEJ on overflight 1, the fluc-
 316 tuations seen by the ground-based magnetometers are not as extreme as the Swarm ob-
 317 servations. Although the cause of this is unknown, it could be due to the ground-based
 318 magnetometers being slightly offset from the magnetic equator. In January 2022, TTB

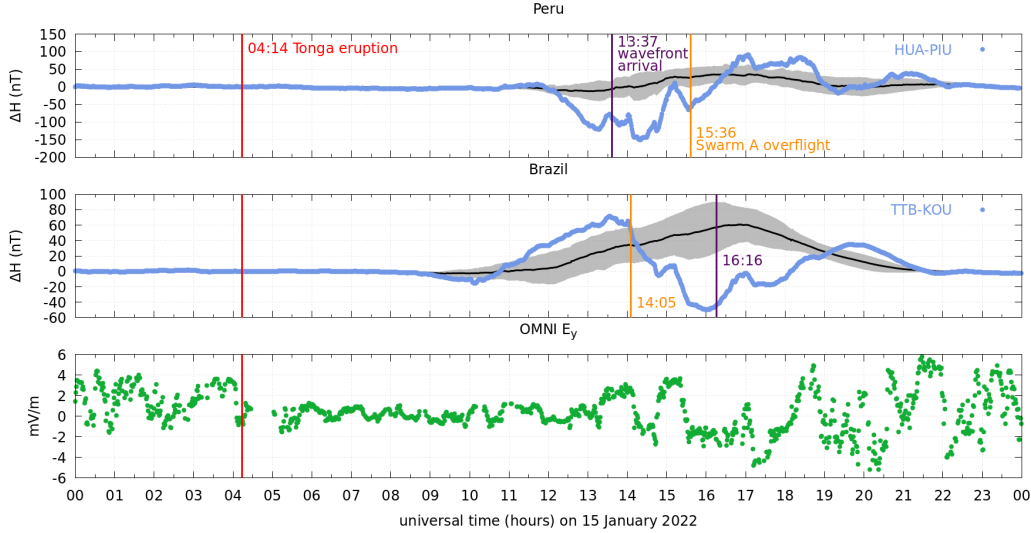


Figure 2. (top) Ground-based magnetometer EEJ intensity estimates over Peru on 15 Jan 2022 computed by subtracting PIU data (off-equator) data from HUA data (on-equator), shown in blue. The monthly mean is in black and ± 1 standard deviation range is in gray. The arrival time of a reference 318 m/s Lamb wavefront (purple line) and time of Swarm overflight (yellow line) are also shown. (middle) Same as top, but for Brazil (TTB - KOU). (bottom) Interplanetary eastward electric field from the OMNI database.

319 and HUA were 2.2° and 0.8° off the magnetic equator according to the CHAOS 7.8 model
 320 (Finlay et al., 2020).

321 The different temporal patterns in Peru and Brazil confirm that the fluctuations
 322 observed by Swarm A are not purely spatial but also temporal. The ground-based mag-
 323 netometer data suggest that the most extreme EEJ activity may have been at locations
 324 and times not sampled by Swarm A (e.g., over Brazil at 16 UT). Future work utilizing
 325 the global network of magnetometers could help elucidate the evolution of global cur-
 326 rents during this event.

327 The magnetometer data show disturbances before the arrival of the 318 m/s Lamb
 328 wavefront (e.g., the negative ΔH in Peru at 13 UT, and the positive and negative ΔH
 329 in Brazil before 16 UT). This is consistent with the Swarm A observations ahead of the
 330 wavefront at 14:05 UT (Figure 1e) and the MIGHTI observations on the first orbit (Fig-
 331 ure 1c, eastward of -60° longitude). It is likely that the thermospheric response to the
 332 eruption is not as simple as the Lamb wave observed in the lower atmosphere, due to
 333 the effects of nonlinear evolution, dispersion, self-acceleration, and secondary wave gen-
 334 eration, among others. Although no numerical models have yet simulated the upper at-
 335 mospheric response to the Tonga Lamb wave, Inchin, Heale, et al. (2020) provide a dis-
 336 cussion on these processes using a first-principles model of the thermospheric signature
 337 of tsunamis.

338 3.4 Geomagnetic storm effects

339 A moderate geomagnetic storm began on 14 Jan 2022; the Tonga eruption and sub-
 340 sequent wave propagation occurred during the recovery phase. It is thus important to
 341 distinguish the signatures caused by the Tonga eruption from the effects of the storm.
 342 The EEJ is known to be modified by electric fields penetrating from the magnetosphere

343 and electric fields originating from the stormtime disturbance dynamo (Yamazaki & Maute,
344 2017, and references therein). First, we rule out penetration electric field effects.

345 Figure 2 (bottom panel) shows the interplanetary electric field (IEF) y-component
346 (dawn-to-dusk electric field) from OMNI data (King & Papitashvili, 2005). The data are
347 taken directly from the OMNI database, except they include a 17-minute delay to ac-
348 count for the delay between the bowshock and the ionosphere (Manoj et al., 2008). If
349 the penetration electric field were the main cause of the EEJ variations, we would ex-
350 pect to see strong correlations between the IEF and ΔH in both longitude sectors. Quan-
351 titatively, the Pearson correlations between IEF and the deviations of ΔH from the monthly
352 mean, (blue lines minus solid black lines in Figure 2), between 8 and 16 hr local time is
353 -0.02 for Peru (13 to 22 UT) and 0.35 for Brazil (11 to 20 UT). However, the fluctua-
354 tions observed in IEF appear to correlate with 1-hour-scale fluctuations observed at both
355 ground-based sites simultaneously (e.g., positive excursions at 15 UT and 17 UT, and
356 possibly at 13.5 UT). After filtering ΔH and IEF to remove their 100-minute running
357 mean, the correlation increased to 0.60 (Peru) and 0.61 (Brazil). Thus, it is likely that
358 the 1-hour-scale fluctuations are caused in part by the penetration electric field, but the
359 larger, longer perturbations of interest here are not. Because of this, and because of the
360 consistency between the EEJ signatures and the neutral wind signatures, as discussed
361 above, we rule out the penetration electric field as the main cause of the extreme east-
362 ward and westward EEJ observed by Swarm.

363 With neutral winds established as the causative mechanism, it is important to rule
364 out geomagnetic activity as the cause of the extreme winds seen in Figure 1(g,h). It is
365 well known that the EEJ can be reversed by the disturbance dynamo, a consequence of
366 westward Coriolis forcing of neutral winds accelerated equatorward by auroral heating
367 (Yamazaki & Maute, 2017). According to the modeling study by Huang et al. (2005),
368 disturbance winds caused by a geomagnetic storm are mainly in the westward direction
369 at middle and low latitudes. MIGHTI observations show both eastward and westward
370 wind perturbations, which are different from the predicted pattern of the disturbance
371 winds. Also, storm-driven wind perturbations are predicted to be much greater at F-region
372 heights (above 150 km) than at E-region heights (below 150 km). MIGHTI observations
373 show large wind perturbations below 150 km (including an eastward perturbation at 100
374 km exceeding 100 m/s), which does not fit the classical picture of the disturbance winds.
375 Furthermore, the westward disturbance wind at mid and low latitudes is stronger dur-
376 ing nighttime than daytime. For instance, Xiong et al. (2015) showed that the average
377 westward disturbance wind at 20–50° latitude is less than 50 m/s for $K_p > 4$ at F-region
378 heights during daytime, while it can exceed 100 m/s during nighttime. Thus, the geo-
379 magnetic storm is unlikely to be the main cause of the extreme daytime winds detected
380 by MIGHTI.

381 The simultaneous occurrence of the Lamb wave arrival, the EEJ signal, and the wind
382 signal, combined with the lack of any significant wind or EEJ signals before this time,
383 represents strong evidence to attribute the observed fluctuations to disturbances caused
384 by the Tonga eruption. Nevertheless, it is possible that high-latitude heating launched
385 traveling atmospheric disturbances during the recovery phase, and it is likely that the
386 longer-term circulation changes caused by the storm have changed the background con-
387 ditions upon which the Tonga signal is superimposed. It will be an interesting topic for
388 future modeling and observational studies to elucidate the interplay of geomagnetic storm
389 and volcanogenic effects on the thermosphere and ionosphere during this period.

390 4 Conclusion

391 The Tonga volcanic eruption caused extreme (>99.9th percentile) fluctuations in
392 the ionospheric wind dynamo, as observed by Swarm and ICON. The relationship be-
393 tween the observed neutral winds and EEJ is consistent with recent theoretical and ob-

servational studies. In particular, the strong westward EEJ (a Hall region current) appears to be driven mostly by westward winds in the Pedersen region. The energy and current paths involved in this nonlocal driving of the EEJ would be an interesting topic for future studies.

Initial reports on the global ionosphere-thermosphere impacts of the Tonga eruption have focused on small- and meso-scale (300–1000 km wavelength) waves seen in TEC at amplitudes of at most a few TEC units, as well as geomagnetic fluctuations 835 km away from and soon after the eruption. The MIGHTI and Swarm observations suggest that modifications of the ionospheric dynamo were extreme relative to background variability, even after ~ 10 hours and $\sim 10,000$ km of wave propagation. This is expected to have caused significant and observable redistributions of ionospheric plasma. As an example of an enormous impulse function, the Tonga eruption may be a useful test for atmosphere-ionosphere coupled models in extreme cases, and the neutral wind and EEJ current signatures reported here could be useful targets.

Acknowledgments

The authors would like to recognize the work of the ICON and Swarm engineering and science teams. ICON is supported by NASA’s Explorers Program through contracts NNG12FA45C and NNG12FA42I. The results presented in this paper rely on magnetic observatory data collected at Huancayo (HUA), Piura (PIU), Kourou (KOU), and Tatuoca (TTB). We thank the Instituto Geofísico del Perú (HUA, PIU), Bureau Central de Magnétisme Terrestre at the Institut de Physique du Globe de Paris (KOU), Observatório Nacional (TTB) and GFZ German Research Centre for Geosciences (TTB) for supporting the operations of these observatories and INTERMAGNET for promoting high standards of magnetic observatory practice (www.intermagnet.org). The authors thank Hermann Lühr, Claudia Stolle, Eileen McIver, and Jonathan Makela for fruitful scientific discussions and suggestions.

Open Research

ICON data can be retrieved from the ICON website (<https://icon.ssl.berkeley.edu/Data>). The European Space Agency (ESA) is gratefully acknowledged for providing Swarm data, which is available from the Swarm website (https://swarm-diss.eo.esa.int/#swarm%2FLevel2daily%2Fentire_mission_data%2FEEF%2FTMS%2FSat_A). The OMNI data were obtained from the GSFC/SPDF OMNIWeb interface at <https://omniweb.gsfc.nasa.gov>. Ground-based magnetometer data from HUA, TTB, and KOU are available from <https://intermagnet.org/data-donnee/download-eng.php>. Data from PIU is available from the LISN network (http://lisn.igp.gob.pe/jdata/view/magnetometer/minute/piur/?itype=magnetometer&dtype=minute&daterange=2022%2F01%2F15+-+2022%2F01%2F15&networks=on&N_IGP=on&N_LISN=on&N_MAGDAS=on&countries=on&C_Argentina=on&C_Brasil=on&C_Colombia=on&C_Peru=on&stations=on&S_areq=on&S_leon=on&S_cuib=on&S_dejp=on&S_huan=on&S_jica=on&S_ancm=on&S_huam=on&S_icam=on&S_nazc=on&S_piur=on&bt_view=piur&S_saol=on&S_tara=on).

References

- Aa, E., Zhang, S.-R., Erickson, P. J., Vierinen, J., Coster, A. J., Goncharenko, L. P., ... Rideout, W. (2022). Significant equatorial plasma bubbles and global ionospheric disturbances after the 2022 tonga volcano eruption. *Earth and Space Science Open Archive*, 17. Retrieved from <https://doi.org/10.1002/essoar.10510637.1> doi: 10.1002/essoar.10510637.1
- Adam, D. (2022). Tonga volcano eruption created puzzling ripples in Earth’s atmosphere. *Nature*, 601, 497. Retrieved from <https://www.nature.com/>

- articles/d41586-022-00127-1 doi: 10.1038/d41586-022-00127-1
- Alken, P. (2020). Estimating currents and electric fields at low latitudes from satellite magnetic measurements. In M. W. Dunlop & H. Lühr (Eds.), *Ionospheric multi-spacecraft analysis tools: Approaches for deriving ionospheric parameters* (pp. 233–254). Cham: Springer International Publishing. Retrieved from https://doi.org/10.1007/978-3-030-26732-2_11 doi: 10.1007/978-3-030-26732-2_11
- Alken, P., Maus, S., Chulliat, A., Vigneron, P., Sirol, O., & Hulot, G. (2015). Swarm equatorial electric field chain: First results. *Geophysical Research Letters*, *42*(3), 673–680. doi: 10.1002/2014GL062658
- Alken, P., Maus, S., Vigneron, P., Sirol, O., & Hulot, G. (2013). Swarm SCARF equatorial electric field inversion chain. *Earth, Planets and Space*, *65*(11), 1309–1317. doi: 10.5047/eps.2013.09.008
- Amores, A., Monserrat, S., Marcos, M., Argüeso, D., Villalonga, J., Jordà, G., & Gomis, D. (2022). Numerical simulation of atmospheric Lamb waves generated by the 2022 Hunga-Tonga volcanic eruption. *Geophysical Research Letters*, 1–8. doi: 10.1029/2022gl098240
- Anderson, D., Anghel, A., Chau, J., & Veliz, O. (2004). Daytime vertical $E \times B$ drift velocities inferred from ground-based magnetometer observations at low latitudes. *Space Weather*, *2*(11), n/a-n/a. doi: 10.1029/2004sw000095
- Aryal, S., Evans, J. S., Correia, J., Burns, A. G., Wang, W., Solomon, S. C., ... Jee, G. (2020). First Global-Scale Synoptic Imaging of Solar Eclipse Effects in the Thermosphere. *Journal of Geophysical Research: Space Physics*, *125*(9). doi: 10.1029/2020JA027789
- Astafyeva, E. (2019). Ionospheric Detection of Natural Hazards. *Reviews of Geophysics*, *57*(4), 1265–1288. doi: 10.1029/2019RG000668
- Bretherton, F. P. (1969). Lamb waves in a nearly isothermal atmosphere. *Quarterly Journal of the Royal Meteorological Society*, *95*(406), 754–757. Retrieved from <https://onlinelibrary.wiley.com/doi/10.1002/qj.49709540608> doi: 10.1002/qj.49709540608
- Englert, C. R., Harlander, J. M., Brown, C. M., Marr, K. D., Miller, I. J., Stump, J. E., ... Immel, T. J. (2017). Michelson Interferometer for Global High-Resolution Thermospheric Imaging (MIGHTI): Instrument Design and Calibration. *Space Science Reviews*, *212*(1-2), 553–584. Retrieved from <http://dx.doi.org/10.1007/s11214-017-0358-4> <http://link.springer.com/10.1007/s11214-017-0358-4> doi: 10.1007/s11214-017-0358-4
- Finlay, C. C., Kloss, C., Olsen, N., Hammer, M. D., Tøffner-Clausen, L., Grayver, A., & Kuvshinov, A. (2020). The CHAOS-7 geomagnetic field model and observed changes in the South Atlantic Anomaly. *Earth, Planets and Space*, *72*(1), 1–31.
- Garrett, C. J. (1969). Atmospheric edge waves. *Quarterly Journal of the Royal Meteorological Society*, *95*(406), 731–753. doi: 10.1002/qj.49709540607
- Harding, B. J., Chau, J. L., He, M., Englert, C. R., Harlander, J. M., Marr, K. D., ... Immel, T. J. (2021). Validation of ICON-MIGHTI Thermospheric Wind Observations: 2. Green-Line Comparisons to Specular Meteor Radars. *Journal of Geophysical Research: Space Physics*, *126*(3), 1–12. Retrieved from <https://onlinelibrary.wiley.com/doi/10.1029/2020JA028947> doi: 10.1029/2020JA028947
- Harding, B. J., Makela, J. J., Englert, C. R., Marr, K. D., Harlander, J. M., England, S. L., & Immel, T. J. (2017). The MIGHTI Wind Retrieval Algorithm: Description and Verification. *Space Science Reviews*, *212*(1-2), 585–600. Retrieved from <http://dx.doi.org/10.1007/s11214-017-0359-3> <http://link.springer.com/10.1007/s11214-017-0359-3> doi: 10.1007/s11214-017-0359-3
- Huang, C.-M., Richmond, A., & Chen, M.-Q. (2005). Theoretical effects of geomag-

- 497 netic activity on low-latitude ionospheric electric fields. *Journal of Geophysical*
 498 *Research: Space Physics*, 110(A5).
- 499 Immel, T. J., England, S. L., Mende, S. B., Heelis, R. A., Englert, C. R., Edelstein,
 500 J., ... Sirk, M. M. (2018). The Ionospheric Connection Explorer Mission:
 501 Mission Goals and Design. *Space Science Reviews*, 214(1), 13. Retrieved from
 502 <http://dx.doi.org/10.1007/s11214-017-0449-2>
 503 [http://link.springer](http://link.springer.com/10.1007/s11214-017-0449-2)
 504 [.com/10.1007/s11214-017-0449-2](http://link.springer.com/10.1007/s11214-017-0449-2) doi: 10.1007/s11214-017-0449-2
- 504 Inchin, P. A., Heale, C. J., Snively, J. B., & Zettergren, M. D. (2020). The Dynam-
 505 ics of Nonlinear Atmospheric Acoustic-Gravity Waves Generated by Tsunamis
 506 Over Realistic Bathymetry. *Journal of Geophysical Research: Space Physics*,
 507 125(12), 1–18. doi: 10.1029/2020JA028309
- 508 Inchin, P. A., Snively, J. B., Zettergren, M. D., Komjathy, A., Verkhoglyadova,
 509 O. P., & Tulası Ram, S. (2020). Modeling of Ionospheric Responses to Atmo-
 510 spheric Acoustic and Gravity Waves Driven by the 2015 Nepal Mw7.8 Gorkha
 511 Earthquake. *Journal of Geophysical Research: Space Physics*, 125(4). doi:
 512 10.1029/2019JA027200
- 513 King, J. H., & Papitashvili, N. E. (2005). Solar wind spatial scales in and
 514 comparisons of hourly Wind and ACE plasma and magnetic field data.
 515 *Journal of Geophysical Research: Space Physics*, 110(A2), 1–9. doi:
 516 10.1029/2004JA010649
- 517 Li, R., Lei, J., & Dang, T. (2021). The Solar Eclipse Effects on the Up-
 518 per Thermosphere. *Geophysical Research Letters*, 48(15), 1–10. doi:
 519 10.1029/2021GL094749
- 520 Lin, J.-T., Rajesh, P. K., Lin, C. C. H., Chou, M.-Y., Liu, J.-Y., Yue, J., ... Kung,
 521 M.-M. (2022). Rapid conjugate appearance of the giant ionospheric lamb wave
 522 in the northern hemisphere after hunga-tonga volcano eruptions. *Earth and*
 523 *Space Science Open Archive*, 27. Retrieved from [https://doi.org/10.1002/](https://doi.org/10.1002/essoar.10510440.2)
 524 [essoar.10510440.2](https://doi.org/10.1002/essoar.10510440.2) doi: 10.1002/essoar.10510440.2
- 525 Makela, J. J., Baughman, M., Navarro, L. A., Harding, B. J., Englert, C. R., Har-
 526 lander, J. M., ... Immel, T. J. (2021). Validation of ICON-MIGHTI Thermo-
 527 spheric Wind Observations: 1. Nighttime Red-Line Ground-Based Fabry-Perot
 528 Interferometers. *Journal of Geophysical Research: Space Physics*, 126(2),
 529 1–29. Retrieved from [https://onlinelibrary.wiley.com/doi/10.1029/](https://onlinelibrary.wiley.com/doi/10.1029/2020JA028726)
 530 [2020JA028726](https://onlinelibrary.wiley.com/doi/10.1029/2020JA028726) doi: 10.1029/2020JA028726
- 531 Manoj, C., Maus, S., Lühr, H., & Alken, P. (2008). Penetration character-
 532 istics of the interplanetary electric field to the daytime equatorial iono-
 533 sphere. *Journal of Geophysical Research: Space Physics*, 113(12), 1–11. doi:
 534 10.1029/2008JA013381
- 535 Nishida, K., Kobayashi, N., & Fukao, Y. (2014). Background Lamb waves in the
 536 Earth's atmosphere. *Geophysical Journal International*, 196(1), 312–316. Re-
 537 trieved from <https://academic.oup.com/gji/article/196/1/312/594635>
 538 doi: 10.1093/gji/ggt413
- 539 Richmond, A. D. (1973). Equatorial electrojet-I. Development of a model including
 540 winds and instabilities. *Journal of Atmospheric and Terrestrial Physics*, 35(6),
 541 1083–1103. doi: 10.1016/0021-9169(73)90007-X
- 542 Soares, G., Yamazaki, Y., & Matzka, J. (2022). Localized geomagnetic disturbance
 543 due to ionospheric response to the hunga tonga eruption on january 15, 2022.
 544 *Earth and Space Science Open Archive*, 12. Retrieved from [https://doi.org/](https://doi.org/10.1002/essoar.10510482.1)
 545 [10.1002/essoar.10510482.1](https://doi.org/10.1002/essoar.10510482.1) doi: 10.1002/essoar.10510482.1
- 546 Themens, D. R., Watson, C., Žagar, N., Vasylyevych, S., Elvidge, S., McCaffrey, A.,
 547 ... Jayachandran, P. (2022). Global propagation of ionospheric disturbances
 548 associated with the 2022 Tonga Volcanic Eruption. *Geophysical Research*
 549 *Letters*. doi: 10.1029/2022gl098158
- 550 Wright, C., Hindley, N., Alexander, M. J., Barlow, M., Hoffmann, L., Mitchell,
 551 C., ... et al. (2022). Tonga eruption triggered waves propagating glob-

- 552 ally from surface to edge of space. *Earth and Space Science Open Archive*,
553 23. Retrieved from <https://doi.org/10.1002/essoar.10510674.1> doi:
554 10.1002/essoar.10510674.1
- 555 Xiong, C., Lühr, H., & Fejer, B. G. (2015). Global features of the disturbance winds
556 during storm time deduced from CHAMP observations. *Journal of Geophysical*
557 *Research A: Space Physics*, 120(6), 5137–5150. doi: 10.1002/2015JA021302
- 558 Yamazaki, Y., Harding, B. J., Stolle, C., & Matzka, J. (2021). Neutral Wind Profiles
559 During Periods of Eastward and Westward Equatorial Electrojet. *Geophysical*
560 *Research Letters*, 48(11), 1–10. doi: 10.1029/2021GL093567
- 561 Yamazaki, Y., & Maute, A. (2017). Sq and EEJ—A Review on the Daily Varia-
562 tion of the Geomagnetic Field Caused by Ionospheric Dynamo Currents. *Space*
563 *Science Reviews*, 206(1-4), 299–405. Retrieved from [http://dx.doi.org/10](http://dx.doi.org/10.1007/s11214-016-0282-z)
564 [.1007/s11214-016-0282-z](http://dx.doi.org/10.1007/s11214-016-0282-z) doi: 10.1007/s11214-016-0282-z
- 565 Yamazaki, Y., Richmond, A. D., Maute, A., Liu, H.-L., Pedatella, N., & Sassi, F.
566 (2014). On the day-to-day variation of the equatorial electrojet during quiet
567 periods. *Journal of Geophysical Research: Space Physics*, 119(8), 6966–
568 6980. Retrieved from <http://doi.wiley.com/10.1002/2014JA020243> doi:
569 10.1002/2014JA020243
- 570 Zettergren, M. D., & Snively, J. B. (2019). Latitude and Longitude Dependence of
571 Ionospheric TEC and Magnetic Perturbations From Infrasonic-Acoustic Waves
572 Generated by Strong Seismic Events. *Geophysical Research Letters*, 46(3),
573 1132–1140. doi: 10.1029/2018GL081569
- 574 Zhang, S.-r., Vierinen, J., Aa, E., & Goncharenko, L. P. (2022). 2022 Tonga vol-
575 canic eruption induced global propagation of ionospheric disturbances via
576 Lamb waves. *Frontiers in Astronomy and Space Sciences*, 9, 1–15. doi:
577 10.3389/fspas.2022.871275